INTERNATIONAL JOURNAL OF HYDROGEN ENERGY 41 (2016) 21965–21978

Available online at www.sciencedirect.com

ScienceDirect

journal homepage: www.elsevier.com/locate/he

# Cobalt nanoparticles imbedded into zeolite crystals: A tailor-made catalyst for one-step synthesis of gasoline from syngas

*Jiangyong Liu* [1], *Dan Wang*, *Jian-Feng Chen* [*], *Yi Zhang*

*Research Centre of the Ministry of Education for High Gravity Engineering and Technology, State Key Laboratory of Organic–Inorganic Composites, Beijing University of Chemical Technology, Beijing 100029, China*

ARTICLE INFO

*Article history:*
Received 8 April 2016
Received in revised form
28 September 2016
Accepted 1 October 2016
Available online 19 October 2016

*Keywords:*
Fischer–Tropsch synthesis
Cobalt
Zeolite
Imbedment
Hydrothermal synthesis
Gasoline

ABSTRACT

The cobalt-imbedded zeolite catalysts in which $Co_3O_4$ particles were compatibly imbedded or confined into the zeolite crystals were prepared with the conventional $Co/SiO_2$ catalyst as the precursor and the silica source by a hydrothermal synthesis method. The effect of hydrothermal condition on the catalyst properties and the catalytic performance for the direct synthesis of gasoline-range hydrocarbons was comparatively investigated in this work. And the formation mechanism for the synthesis of this kind of catalyst was proposed. The coincidence of the rate of the silica dissolving process and the zeolite crystallization process was proved to be the key to the rational design of this imbedment-structured catalyst. Compared with the conventional $Co/SiO_2$ catalyst and the zeolite-supported catalyst, the optimized cobalt-imbedded zeolite catalysts present significantly higher gasoline selectivity and produce more *iso*-paraffins, which can be reasonably attributed to the confined reaction environment, the high diffusion efficiency, the proper reduction behavior, and the suitable acidic properties.



## Introduction

Fischer–Tropsch Synthesis (FTS) has attracted considerable attention as an alternative route for obtaining clean fuel and valuable chemicals via conversion of syngas (a mixture of CO and $H_2$) derived from abundant and renewable sources since the pioneering work of Franz Fischer and Hans Tropsch [1–5]. The resurgence of interest in FTS has been primarily motivated by the problems of utilization of stranded gas, diversification of sources of fossil fuels, and environmental concerns [1]. Comparing with the fuels derived from petroleum or crude oil, gasoline or diesel from FTS generally behaves with sulfur-free, aromatic-free and nitrogen-free properties [2]. Despite all the advantages, with respect to the production of synthetic gasoline, the FTS process mainly suffers from two constraints. On one hand, originating from the polymeric nature of the reaction, the carbon number distribution of the products (from methane to long-chain hydrocarbons) obeys the Anderson-Schulz-Flory (ASF) distribution, characterized by a parameter $\alpha$ known as the chain growth probability. Therefore, the selectivity of gasoline-range hydrocarbons is theoretically limited to a maximum value of about 45%. On the other hand, the dominating *n*-paraffins in the FTS products

* *Corresponding author*. Fax: +86 10 64434784.
E-mail address: chenjf@mail.buct.edu.cn (J.-F. Chen).
[1] Present address: College of Chemistry and Chemical Engineering, Yangzhou University, Yangzhou, Jiangsu 225002, China.
http://dx.doi.org/10.1016/j.ijhydene.2016.10.004
0360-3199/

determine too poor quality of the synthetic gasoline with low octane number, which means extensive downstream procedures are required to upgrade the liner hydrocarbons into high-octane structured components [1,2].

In order to overcome the above two limitations of the FTS oriented to the synthesis of gasoline, the utilizing of the multiple functionalities of zeolites in the reaction system is one of the main focuses to circumvent the selectivity limitation and quality problem. Recently, tremendous efforts have been devoted to the preparation of bifunctional catalysts combined of conventional FTS catalysts with zeolites as co-catalysts, aiming at directly obtain hydrocarbons with certain carbon number distribution. The zeolite component in the composite catalysts can promote the secondary reactions (e.g., hydrocracking, isomerization, oligomerization) of the primary products formed on the FTS catalysts in the production of high-octane branched and aromatic hydrocarbons, resulting in enhanced gasoline selectivity with non-ASF distributions. Some researchers have attempted to prepare catalysts with FTS active metal supported on an acidic zeolite, generally by the procedures of impregnation, drying and calcination [6,7]. Although the preparation techniques have great practical simplicity, these catalysts usually exhibited low FTS activity, extremely bad reduction degree and relatively high methane selectivity. On the other hand, the hybrid catalysts, physically mixed by FTS catalysts (e.g., $Co/SiO_2$, fused iron) and zeolites (e.g., HZSM-5, Hβ) have been employed to directly convert syngas into isoparaffins [8–10]. In this catalyst system, the heavy products such as wax formed on the FTS catalysts can be hydrocracked and isomerized to branched hydrocarbons on the neighboring acidic sites of zeolites. However, the yield of isomerized products is not high enough. Despite the improved selectivity of short-chain hydrocarbons, partial long-chain hydrocarbons can desorb directly and escape without contacting the catalytically acidic sites, which is believed that the reactions of hydrocracking and isomerization occurring on the zeolite are random [11].

To further promote the *iso*-paraffin selectivity, novel zeolite capsule catalyst with a core–shell structure has been developed in our previous reports [12,13]. The capsule catalyst consisted of a FTS catalyst such as $Co/SiO_2$ as the core and a layer of zeolite membrane such as HZSM-5 as the shell, providing spatially confined effects and shape selectivity properties. During the FTS reaction, syngas firstly passes through the zeolite to reach the inner core catalyst, and then all the formed straight-chain hydrocarbons must pass through the zeolite channels to be converted to *iso*-paraffins. As a result of this confined reaction field, the selectivity of *iso*-paraffins was improved dramatically, and the formation of heavy paraffins ($C_{12+}$) was completely suppressed [12]. However, the zeolite membrane is directly coated on the millimeter-sized $SiO_2$-supported or $Al_2O_3$-supported catalyst in a strong basic condition, resulting in ultimately unsatisfactory mechanical stability. In addition, the pretreatment of the precursor catalyst is always time-consuming and complicated.

Herein, we developed an intriguing cobalt-imbedded zeolite catalyst, prepared with conventional $Co/SiO_2$ catalyst as the precursor of the zeolite by a facile hydrothermal method. With this strategy, the imbedment of cobalt particles into the zeolite crystal was successfully achieved, as confirmed by various characterization techniques. This tailor-made catalyst not only significantly promoted the selectivity of gasoline-range hydrocarbons, but also exhibited excellent stability and high catalytic activity for the FTS oriented to the one-step synthesis of gasoline. In addition, the effect of the hydrothermal condition of the preparation system was stressed and elucidated to gain insights into the synthesis mechanism of this imbedment-structured catalyst. The coincidence of the rate of the silica dissolving process and the zeolite crystallization procedure is proved to be the key to the rational design of this high-performance catalyst.

## Experimental section

### *Catalyst preparation*

#### *Preparation of precursor catalyst*

The support for the preparation of conventional $Co/SiO_2$ catalyst was commercially available $SiO_2$ (specific surface area 451 $m^2 g^{-1}$, pore volume 1.061 $cm^3 g^{-1}$ and average diameter of pore 6.7 nm). Employing the incipient wet impregnation method, the aqueous solution containing the required amount of $Co(NO_3)_2 \cdot 6H_2O$ was used to yield nominal 20 wt% cobalt loading. Then the catalyst was vacuuming for 1 h and dried at 393 K for 12 h. Thereafter, the catalyst precursor was calcined in air from room temperature to 673 K for 2 h, with a ramping rate of 2 K $min^{-1}$.

#### *Preparation of cobalt-imbedded zeolite catalysts*

For the one-step preparation of cobalt-imbedded zeolite catalysts with $Co/SiO_2$ as the precursor, hydrothermal synthesis was employed. Tetrapropylammonium hydroxide (TPAOH) was selected as the structure-directing agent. For the crystallization of the zeolite, the Si source originated from the gradually dissolved silica from $Co/SiO_2$ during the synthesis process, while $Al(NO_3)_3 \cdot 9H_2O$ served as the Al source. The synthesis recipe was based on the molar ratio of 0.3 TPAOH: 10 EtOH: 0.025 $Al(NO_3)_3$: 1.0 $SiO_2$: 32$H_2O$. The nominal molar ratio of Si/Al in this study was 40. It should be noted that in this work $NH_3 \cdot H_2O$ (ammonia aqueous solution) was selected as the alkali source to enforce and control the silica dissolving process in the crystallization and growth of the zeolite [14,15].

$Al(NO_3)_3 \cdot 9H_2O$ was firstly dissolved with deionized water and high-purity ethanol under continuous stirring in a stainless steel autoclave with a Teflon inner tank. After that, the precursor catalyst powder and the template TPAOH were added into the solution. Subsequently, the reaction mixture was sealed in the Teflon container with vigorous stirring for 6 h at room temperature. Afterwards, different volume of $NH_3 \cdot H_2O$ was added into the mixture and stirred continuously for another 15 min. Finally, the hydrothermal process was performed at 453 K for a crystallization time of 100 h. The obtained samples were filtered from the mother liquid and washed thoroughly with deionized water and ethanol, followed by drying at 393 K for 12 h. Calculation in air from room temperature to 773 K for 5 h with a ramping rate of 2 K $min^{-1}$ was conducted in order to remove the organic structure-directing agent that had stored in the zeolite pores.

The obtained catalysts were denoted as CoZ-xN, where x stands for the dosage of ammonia and represented by the molar ratio of $n(NH_3 \cdot H_2O)/n[Al(NO_3)_3 \cdot 9H_2O]$. The direct synthesis of proton-type HZSM-5 was also performed through the hydrothermal process as mentioned above, with the same Al source, structure-directing agent and molar composition. The only difference was that the silica source was pure $SiO_2$, and the obtained pure HZSM-5 zeolites were denoted as Z-xN. It should be noted that prior to each preparation process the inner tanks were carefully washed with NaOH aqueous solution at 453 K for 4 h to avoid adventitious zeolite seeding, followed by dilute nitric acid and deionized water.

*Preparation of zeolite-supported cobalt catalyst*

Self-made Z-300N powder (molar ratio of Si/Al = 40, molar ratio of $n(NH_3 \cdot H_2O)/n[Al(NO_3)_3 \cdot 9H_2O] = 300$) was utilized as a support for the preparation of the zeolite-supported catalyst, denoted as Co/Z. The Co/Z catalyst with nominal 20 wt% cobalt loading was prepared by impregnating the as-obtained Z-300N support with excessive $Co(NO_3)_2 \cdot 6H_2O$ aqueous solution. Afterwards, the suspension was continuously stirring overnight at room temperature. Before drying and calcination, the mixture was heated at 333 K to remove the residual water.

### Catalyst characterization

An X-ray diffractometer (Rigaku D/max − 2500VB2+/PC) equipped with Cu Kα radiation (λ = 0.154056 nm) was employed to record the powder X-ray diffraction (XRD) patterns within the 2θ range of 5–90°. The X-ray tube was operated at 40 kV and at 200 mA. The supported crystalline size of cobalt oxide of the catalysts was evaluated with the help of Scherrer equation by using the full-width at half maximum (FWHM) of the diffraction peak of $Co_3O_4$ crystallites at 2θ of 59.3° instead of the commonly used 36.9° to avoid the disturbance of the diffraction peaks of HZSM-5. The crystal size of the metallic cobalt of the reduced catalysts was calculated with the help of the equation of $d\,(Co^0) = 0.75 \cdot d\,(Co_3O_4)$. And the crystallinity of the zeolite-involved samples was determined by the calculation as following: (peak area between 2θ = 22–25° of the sample/peak area between 2θ = 22–25° of the reference) × 100%. The zeolite with the maximum peak area between 2θ = 22–25° was selected as a reference and defined as a crystallinity of 100%.

The Fourier-transform infrared (FT-IR) spectra of the samples were obtained with a Nicolet Model 205 spectrometer. The sample was mixed with KBr and the mixture was then pressed into thin wafers.

The elemental compositions of the various catalysts were determined by X-ray fluorescence (XRF) on a XRF-1800 spectrometer.

The morphology of the samples was investigated with a field-emission scanning electron microscope (SEM) (Hitachi S-4700), combined with an energy-diffusive X-ray spectroscopy attachment (EDAX, Genesis 60), which can simultaneously provide the elemental composition analysis. EDS mapping was performed on a scanning electron microscope (JEOL JSM-7800F) equipped with an attachment (OXFORD X-Max, Oxford Instruments, Oxford, UK). The samples used for this analysis were first deposited on a holder with an adhesive carbon tape and then coated by a platinum layer on the surface.

Transmission electron microscopy (TEM) images were obtained on a JEOL JEM-3010 microscope. The samples were prepared in an ultrasonic bath with ethanol as the dispersing agent. Then a drop of the suspension was deposited on a copper grid covered with a carbon perforated film and the solvent was allowed to evaporate. The size distribution of $Co_3O_4$ nanoparticles was measured from the statistical TEM data over 150 selected particles via several high magnification images.

The high-angle annular dark-field scanning-transmission electron microscopy (HAADF-STEM) image was obtained on a Tecnai G2 F20 S-Twin high-resolution TEM. The sample preparation was similar with the TEM analysis.

$^{27}Al$ solid-state nuclear magnetic resonance ($^{27}Al$ NMR) spectra of the calcined catalysts packed in a $ZrO_2$ NMR rotor were recorded under magic angle spinning (MAS) in a 300 MHz solid-state Bruker AV300 spectrometer ($B_0 = 7.05$ T). The MAS-NMR spectra were obtained with a frequency of 78.2 MHz, a spinning rate of 8.0 kHz, and a recycling delay of 0.5s.

The acidic properties of the FTS catalysts were measured by the temperature-programmed desorption of ammonia ($NH_3$-TPD). Before the analysis, about 0.1 g of the calcined samples were loaded in a quartz micro-reactor and then pretreated with a He flow at 473 K for 1 h. After cooling to 373 K, ammonia was introduced into the reactor and the adsorption process was performed at 373 K for 1 h. Prior to the desorption process, the samples were purged with He again to remove the gaseous and physically adsorbed $NH_3$ at 373 K for 30 min. The TPD experiments were then carried out under a He flow rate of 50 mL/min from 373 K to 923 K at a ramping rate of 10 K $min^{-1}$. The effluent was detected by on-line gas chromatograph with a thermal conductivity detector.

The hydrogen temperature programmed reduction ($H_2$-TPR) experiments were conducted in a quartz-made micro-reactor using 0.1 g calcined catalysts. The samples were reduced with a mixture of 10% $H_2$/Ar (vol.) in a flow rate of 30 mL $min^{-1}$. The temperature was raised from 323 K to 1173 K with a linear heating rate of 10 K $min^{-1}$. After passing through a 5A molecular sieve trap to remove the generated water during the reduction, the effluent gas was detected by a thermal conductivity detector.

### Catalytic reaction

The FTS reactions were carried out in a continuous-flow-type fixed-bed reactor. The catalysts were first pressurized and sieved to the desired grains of 20–40 mesh. The catalysts diluted with quartz sands were loaded in the center of the stainless steel reactor and reduced in situ at atmospheric pressure in the flow of pure $H_2$ (80 mL $min^{-1}$) at 673 K for 10 h, and then cooled down to about 373 K before switching to syngas. The temperature and pressure of the FTS reaction were 533 K and 1.0 MPa, respectively. The molar ratio of $H_2$/CO was 2 and $W_{catalyst}/F_{syngas}$ was 5 g h $mol^{-1}$. All the transfer lines between the outlet of the reactor and the inlet of the gas chromatography were heated at about 473 K to prevent the possible condensation of heavy compounds. The effluent gas released from the reactor during the reaction process was

analyzed by online gas chromatography (Shimadzu, GC-2014C). The concentration of CO and $CO_2$ in the effluent were analyzed with a thermal conductivity detector (TCD) equipped with an active charcoal column. The product was also analyzed by a flame ionization detector (FID) for gaseous hydrocarbons (Porapak Q, online) and for liquid hydrocarbons (SE-30, uniport), respectively. In addition, the condensate hydrocarbons collected in an ice trap were analyzed with the GC-FID equipped with a capillary column (J&W Scientific GS-Alumina, i.d. 0.53 mm, length = 30 m) for separating the iso- and *n*-paraffins. All the analysis results mentioned above were summed up to obtain the composition of the corresponding hydrocarbons. The selectivity and the CO conversion were calculated using the reaction data at 30 h. The product selectivity in the reaction system was calculated in terms of carbon mol percentage (c-mol %). Argon was selected as an internal standard, with a concentration of 5% in the feed gas.

The conversion percentage of CO was calculated as the following:

$$\text{CO conversion } (\%) = \frac{\left(\frac{CO}{Ar}\right)_{in} - \left(\frac{CO}{Ar}\right)_{out}}{\left(\frac{CO}{Ar}\right)_{in}} \times 100\%$$

The selectivity of hydrocarbon component ($C_i$) was demonstrated as the following:

$$\text{Selectivity of } (\%) = \frac{\text{molar number of } C_i}{\sum C_i} \times 100\%$$

## Results and discussion

### *Phase, texture and morphologies*

Fig. 1 shows the XRD patterns of the impregnated catalyst Co/$SiO_2$, the zeolite-supported catalyst Co/Z and the series cobalt-imbedded zeolite catalysts CoZ-xN. All peaks displaying a flat baseline can be indexed to the crystalline $Co_3O_4$ spinel phase

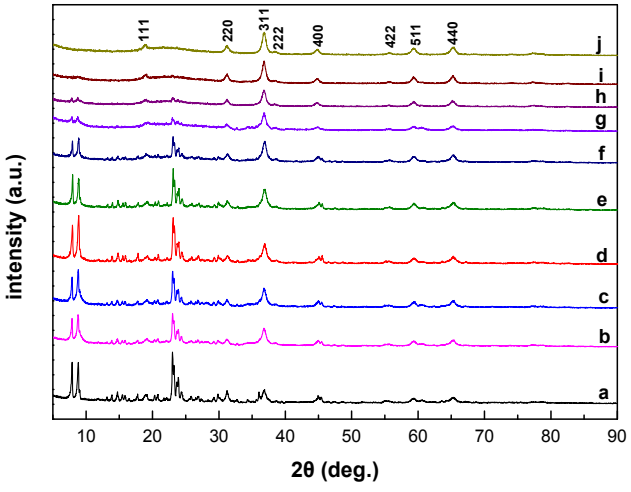


**Fig. 1 – XRD patterns of the samples: (a) Co/Z, (b) CoZ-500N, (c) CoZ-400N, (d) CoZ-300N, (e) CoZ-200N, (f) CoZ-100N, (g) CoZ-50N, (h) CoZ-15N, (i) CoZ-0N and (j) Co/$SiO_2$.**

and MFI-type HZSM-5, with no other crystalline phases observed, thereby confirming the high purity of the materials. The relative zeolite crystallinity of the catalysts as listed in Table 1 and presented in Fig. S1 is significantly dependent on the ammonia content, i.e. basicity of the hydrothermal system. As shown in Fig. S1, the crystallinity of the HZSM-5 zeolite is progressively increased from CoZ-0N to CoZ-200N and achieves the highest value in the CoZ-300N catalyst. As shown in Fig. 1, the wide diffraction peak of amorphous silica centered at about 20° for CoZ-xN catalysts gradually weakens and finally disappears. This indicates that with increasing the basicity, the vast majority of Si in the precursor Co/$SiO_2$ was dissolved to act as Si source and was finally transformed into the framework of HZSM-5. It seems that the larger the amount of ammonia addition, the more prone to obtain highly crystallized HZSM-5 catalysts. However, this is not true since the zeolite crystallinity is gradually decreased from CoZ-300N to CoZ-500N. Therefore, excessive ammonia addition or too high basicity cannot facilitate the improvement of the zeolite crystallinity, but instead can hinder the zeolite nucleation process [16]. In fact, after the hydrothermal reaction, almost no silica species were detectable in the resulting solution collected from the autoclave except for CoZ-400N and CoZ-500N catalysts, implying that some silica species were not converted into the zeolite and finally leached out from the mixture in these two catalysts. It should be noted that the cobalt content in the final catalyst should be close to that of the Co/$SiO_2$ precursor, i.e. 20 wt%, considering the very small amount of aluminum added to the synthetic solution. This is verified by the cobalt content of the CoZ-xN catalysts (x = 0, 15, 50, 100, 200, 300), as determined by XRF analysis (Table 1), which is consistent with the theoretical value. However, in the case of CoZ-400N and CoZ-500N catalysts, the cobalt content is 22.1 wt% and 23.4 wt%, respectively, apparently higher than 20 wt%. This observation strongly supports our explanation on the silica loss and weight reduction of these two catalysts.

The variation in the zeolite crystallinity can also be reflected in the FT-IR spectra of the pure HZSM-5 samples, as shown in Fig. S2, where the band at about 548 $cm^{-1}$ assigned to the asymmetric stretching vibration of $SiO_4$ tetrahedra determines the materials are of MFI type [17]. For the Z-0N sample, almost no peak at 548 $cm^{-1}$ can be distinguished, indicating its very low zeolite crystallinity. Furthermore, the intensity ratio of the band 548 $cm^{-1}$ to 450 $cm^{-1}$ ($I_{548}/I_{450}$) can be utilized to assess the named IR crystallinity of the samples [18]. The maximum $I_{548}/I_{450}$ value (0.75) is obtained on the Z-300N catalyst, suggesting the high ordering of the HZSM-5 material, considering that the optical density ratio of pure pentasil is 0.8 [18].

The estimated crystallite sizes of $Co_3O_4$ in the catalysts were also calculated from the XRD line broadening with the Scherrer equation and exhibited in Table 1. Irrespective of the different hydrothermal conditions, the average crystal sizes of $Co_3O_4$ and metallic cobalt of the CoZ-xN catalysts are just slightly varied in a narrow range and close to those of the Co/$SiO_2$ catalyst, indicating that the size and distribution of $Co_3O_4$ particles in the precursor tend to be retained after the hydrothermal treatment and calcination process. In the case of the impregnated Co/Z catalyst with the self-made HZSM-5 as a support (Fig. 1a), however, the diffraction peaks of $Co_3O_4$

**Table 1 – Properties of the catalysts.**

| Catalyst | $Co_3O_4$ particle size/nm | | HZSM-5 crystallinity/% | XRF | | Co particle size/nm[d] |
|---|---|---|---|---|---|---|
| | I[a] | II[b] | | Co content/%[c] | Si/Al ratio[c] | |
| $Co/SiO_2$ | 13.7 | 12.8 | – | 20.5 | – | 10.3 |
| CoZ-0N | 13.8 | 12.4 | 2.1 | 20.0 | 41.7 | 10.4 |
| CoZ-15N | 13.8 | 11.8 | 9.3 | 20.6 | 40.8 | 10.4 |
| CoZ-50N | 13.1 | 12.1 | 15.8 | 20.5 | 38.5 | 9.8 |
| CoZ-100N | 13.8 | 11.0 | 47.1 | 20.8 | 38.9 | 10.4 |
| CoZ-200N | 13.2 | 11.4 | 74.4 | 20.6 | 37.2 | 9.9 |
| CoZ-300N | 13.0 | 12.1 | 90.6 | 20.9 | 36.8 | 9.8 |
| CoZ-400N | 13.1 | 12.5 | 69.9 | 22.1 | 38.7 | 9.8 |
| CoZ-500N | 13.6 | 12.5 | 62.9 | 23.4 | 39.3 | 10.2 |
| Co/Z | 7.8 | 5.1 | 100 | 20.2 | 37.0 | 5.9 |

[a] Calculated by XRD pattern.
[b] Evaluated from TEM image.
[c] Calculated from XRF data.
[d] Measured by the equation $d\ (Co^0) = 0.75 \cdot d\ (Co_3O_4)$ and the $Co_3O_4$ particle size calculated by XRD pattern.

were found to be apparently broadened, implying a considerably smaller $Co_3O_4$ particle size.

Fig. 2 shows the typical SEM images of the CoZ-xN catalysts. HZSM-5 zeolite with classical morphology of hexagonal-prism shaped crystals, with the longest crystal dimension along the c-axis, can be observed from all the samples. Only slight differences in the size and shape of individual zeolite crystallites can be distinguished. Nevertheless, some amorphous silica species still exist in the CoZ-15N and Co-100N catalysts, indicating a relatively low crystallinity, which is consistent with the XRD results (Fig. 1 and Table 1). For the CoZ-300N catalyst, it is consisted of regular HZSM-5 crystals, with almost no other morphologies observable, demonstrating good uniformity and high crystallinity. However, further increase of the ammonia quantity of the hydrothermal process will not be beneficial to the powder morphology, as represented in the CoZ-500N catalyst, where the zeolite crystals become somewhat irregular and fragile.

The typical TEM images of the various catalysts are exhibited in Fig. 3. It can be clearly observed that distinguishable $Co_3O_4$ clusters or aggregates are suitably imbedded or confined into the HZSM-5 crystals and are homogeneously distributed with a good degree of dispersion (Fig. 3c–e). Based on the particle size distributions obtained from the TEM images with high magnifications, the average $Co_3O_4$ particle sizes of the series CoZ-xN catalysts were calculated, and all the values are in the range of 11.0–13.0 nm (Table 1), similar to that of the precursor $Co/SiO_2$ catalyst and slightly lower than the XRD calculation results. These results indicate that the $Co_3O_4$ particles in the precursor were preserved with minor changes and prevented from apparent aggregating or migration during the hydrothermal preparation and calcination process, which further demonstrates that the cobalt-imbedded structure is well organized and very stubborn since the $Co_3O_4$ particles were compatibly imbedded into the zeolite crystals. This finding can be further corroborated by the representative HAADF-STEM image of the CoZ-300N catalyst (Fig. 3c inset). Compared with the CoZ-xN catalysts, the Co/Z catalyst present more dispersed $Co_3O_4$ particles (Fig. 3b), with an average particle size of 5.1 nm, which is the smallest among all the catalysts and in accordance with the XRD analysis.

### *Acid properties of the catalysts*

Since aluminum is the origin of the Brönsted acidity of aluminosilicate molecular sieves, its quantity, location and coordination state are of much interest, and should be comprehensively investigated. The bulk molar ratios of Si/Al for the various CoZ-xN catalysts were determined by the XRF analysis (Table 1). It is interesting to find that all the bulk Si/Al ratios are in the range of 36–42, which are very similar with the nominal value of the primary synthetic solution, in spite of the different hydrothermal details. Therefore, it is rationally concluded that almost all of the aluminum species were brought into the catalysts via the hydrothermal treatment, regardless of the relative amount of aluminosilicate zeolites and amorphous silica in the final catalysts. This means that in the catalysts with low zeolite crystallinity such as CoZ-0N, aluminum species also exist on the undissolved amorphous silica.

Although the aluminum source is effectively utilized in the series CoZ-xN catalysts, the state of aluminum in the catalysts is not distinguished. To investigate the difference of the surroundings of aluminum in the catalysts, solid-state $^{27}Al$ MAS NMR studies were carried out, with the spectra presented in Fig. 4. The strong signals with the maximum chemical shifts of about 54 ppm are typically attributed to the tetrahedrally coordinated framework Al (FAL) atoms located in the zeolite matrix [19]. For CoZ-0N, CoZ-15N and CoZ-50N catalysts, apparent octahedrally coordinated Al atoms characterized by resonances at about 0 ppm were detected, indicating that extra-framework aluminum (EFAL) species were formed [19]. And some amorphous Al (AAL) appears in the poorly crystallized CoZ-xN samples such as CoZ-0N, as confirmed by the protruded baseline, implying that aluminum was not only converted into the zeolite crystal but also dispersed on the undissolved silica [20], just as stated above. This is also clearly supported by the EDS analysis that aluminum was detected in the undissolved amorphous material of the CoZ-15N catalyst (Fig. 1h). Moreover, the broadening of the FAL peak in these samples can be attributed to the decreased symmetry of some aluminum sites [21]. Such finding is not surprising since it is difficult to synthesize

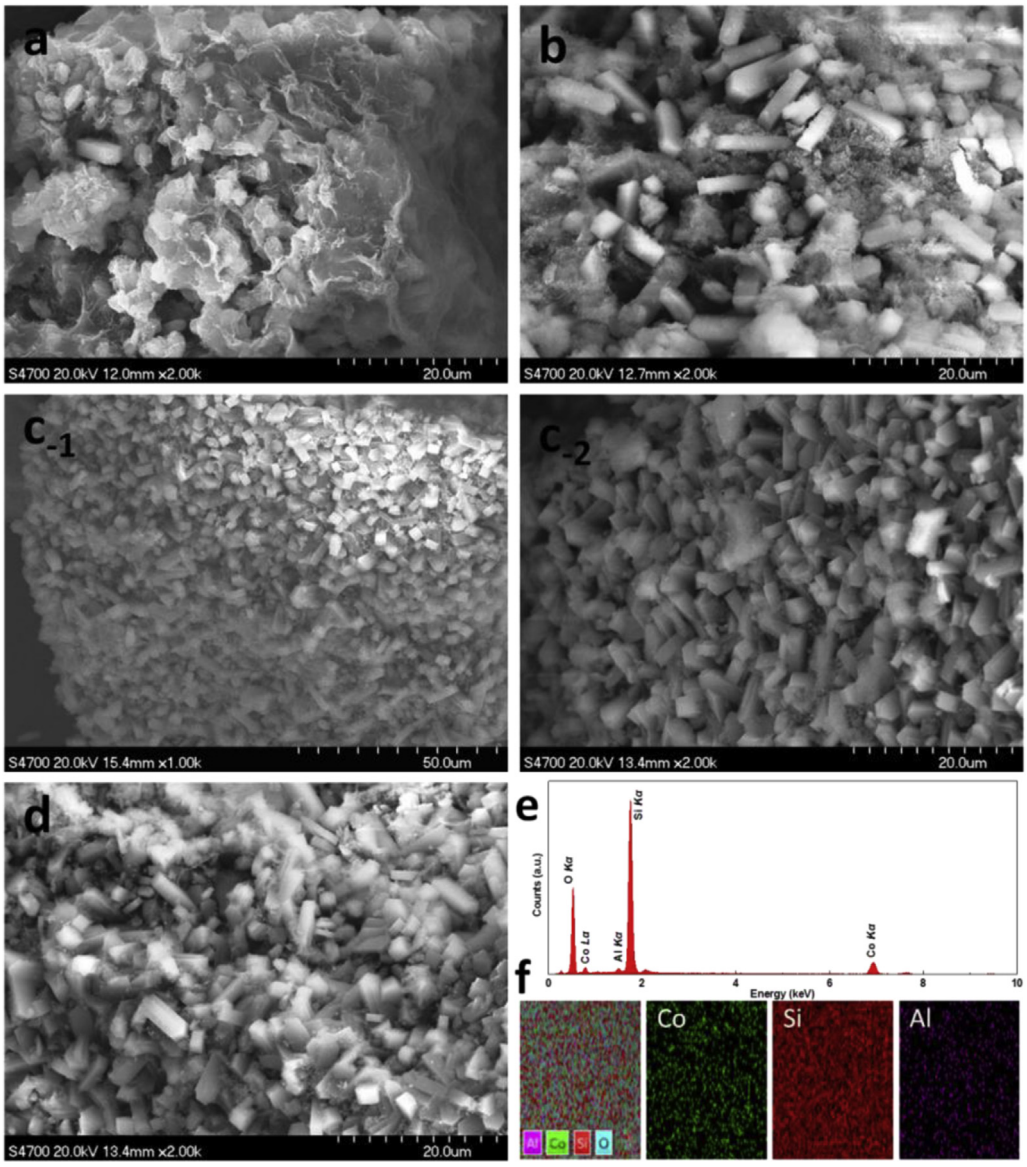


**Fig. 2 – SEM images of the catalysts: (a) CoZ-15N, (b) CoZ-100N, (c) CoZ-300N and (d) CoZ-500N catalysts. EDS spectrum (e) and elemental mapping (f) of an individual zeolite crystallite in the CoZ-300N catalyst.**

HZSM-5 with very high Al content, thus incorporation of all aluminum into the zeolite crystals of the catalysts with low zeolite crystallinity is unpractical. The absence of EFAL and AAL species in the highly crystallized CoZ-200N to CoZ-500N catalysts suggests that the vast majority of the Al species have been effectively converted into the HZSM-5 framework. Selected EDS analysis of the representative zeolite crystal in the CoZ-300N catalyst is displayed in Fig. 2e, and the calculated molar Si/Al ratio is 38.0, which is in line with the nominal value (40) and close to the XRF result (36.8). Moreover, the EDS elemental mapping performed on an individual zeolite crystal reveals the homogeneous element distribution of cobalt, silicon and aluminum in the CoZ-300N catalyst. It is rationally expected that the quantity, location, and coordination state of aluminum should have a great influence on the acidic property of the catalysts, which were further investigated with the help of the $NH_3$-TPD technique.

Fig. 5 shows the $NH_3$-TPD results. As indicated from the profiles, all the samples display two main desorption peaks except for $Co/SiO_2$, which shows trace amount of acidic sites. The low temperature (LT) peak centered at about 500 K and the high temperature (HT) peak centered at about 760 K are assigned to the weak acidic sites and strong acidic sites, respectively [22]. Among all the CoZ-xN catalysts, CoZ-300N shows the highest HT peak, corresponding to the presence of the largest quantity of acidic sites while CoZ-0N catalyst gives the lowest one. This result is easy to understand when the zeolite crystallinity and the aluminum properties of the CoZ-xN catalysts are considered, as fully discussed above. It is well known that the Brönsted acidity of the aluminosilicate zeolite stems from the presence of accessible hydroxyl groups associated with FAL atoms ("structural hydroxyls") [23]. EFAL species, however, are generally considered to be associated with the amount of acidic sites that are hardly active in the

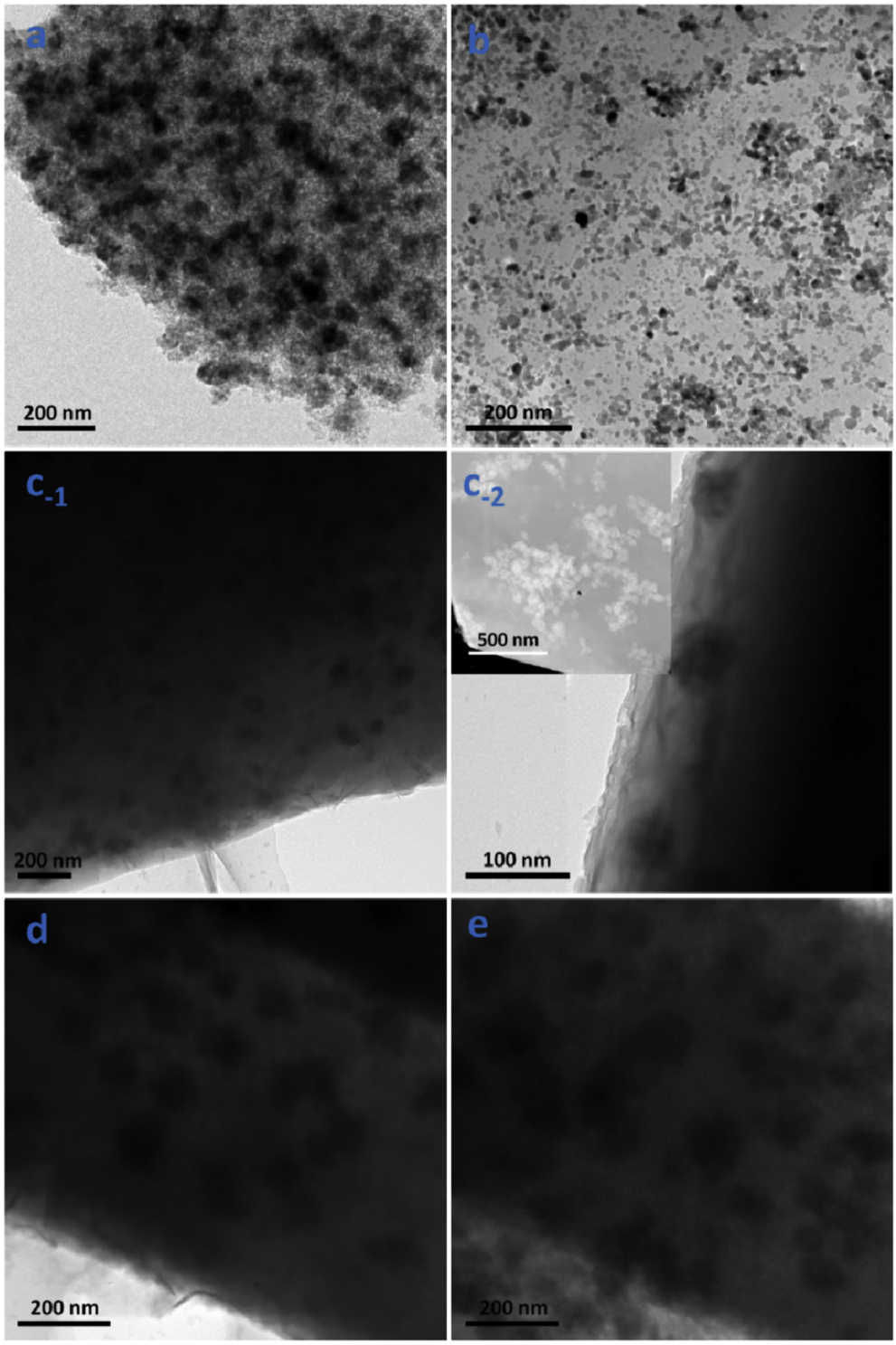


**Fig. 3 – TEM images of the catalysts: (a) Co/$SiO_2$, (b) Co/Z, (c) CoZ-300N, (d) CoZ-200N and (e) CoZ-500N catalysts. The insert in (c) is the selected HAADF-STEM image.**

cracking and isomerization of heavy hydrocarbons [24]. Therefore, the CoZ-300N catalyst with the best zeolite crystallinity and fine framework aluminum atoms should possess the most acidic sites, while the contrary result is observed for the poorly crystallized CoZ-0N catalyst in which EFAL and amorphous aluminum have been proved to exist. For the CoZ-500N catalyst, the decreased acidity should be attributed to the deteriorative effects of excess ammonia as discussed above. In the case of the Co/Z catalyst with the self-made acidic HZSM-5 powder as the support, more acidic sites can

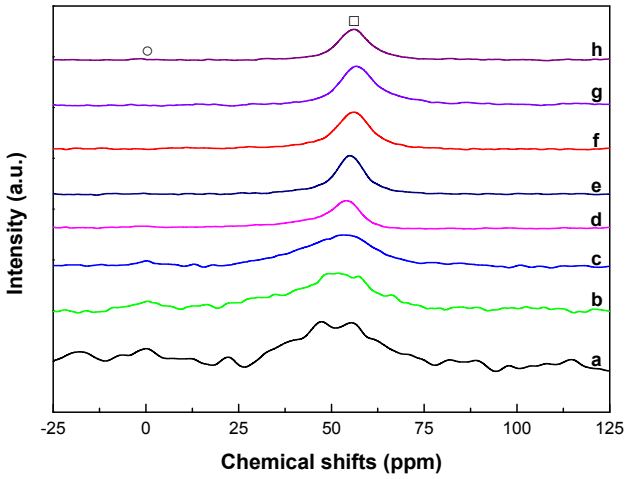


**Fig. 4 – $^{27}$Al NMR spectra of the catalysts: (a) CoZ-0N, (b) CoZ-15N, (c) CoZ-50N, (d) CoZ-100N, (e) CoZ-200N, (f) CoZ-300N, (g) CoZ-400N and (h) CoZ-500N. (□) tetrahedral aluminum, (○) octahedral aluminum.**

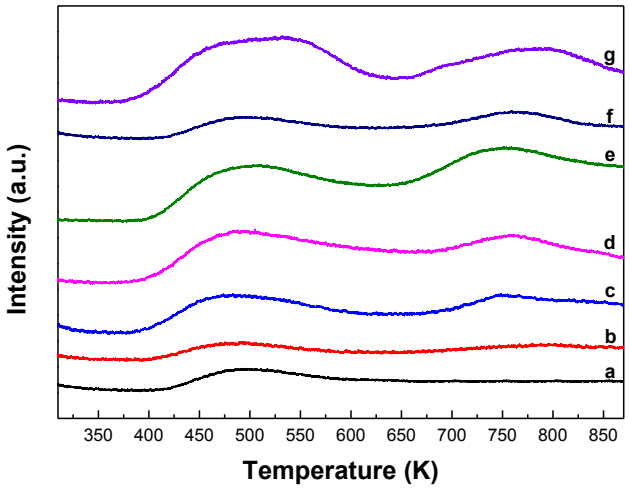


**Fig. 5 – $NH_3$-TPD profiles of the calcined catalysts: (a) Co/$SiO_2$, (b) CoZ-15N, (c) CoZ-100N, (d) CoZ-200N, (e) CoZ-300N, (f) CoZ-500N and (g) Co/Z catalysts.**

be obtained as the intensity of the two desorption peaks is observed to be apparently larger than that of the CoZ-300N catalyst, which could be derived from the different preparation method that involves impregnation, drying and calcination processes.

### *Proposed formation mechanism*

Theoretically, Oswald's proposed rule of successive transformations states that a metastable silicate phase will successively transform to more stable (denser) phases until it reaches the most stable phase [25]. This concept indicates that the recrystallization of silica to ZSM-5 is possible in principle [26]. It's worth noting that the reactants were selected carefully in this study to avoid unwanted deactivation of the obtained catalysts. With this in mind, the frequently used strong base NaOH should not be utilized, and the related impurities should not be present in the raw materials used for the synthesis. In addition, the conventional tedious method for synthesizing proton-type zeolite by ion-exchange of Na-type zeolite should not be applied in our study since even small amounts of Na can be a poison for FTS process and deactivate the catalysts [27], although Na was reported to be able to accelerate the zeolite crystallization process [28]. What's more, compared with the harsh environment of NaOH and the like, the silicon dissolution by the controlled-released hydroxyl from the weak inorganic base ammonium hydroxide is much milder [29]. This mild silica dissolving process is of benefits for coinciding with the crystallizing process of the zeolite. Thus, this further indicates that the addition of ammonia to the hydrothermal system plays an extremely important role in the successful synthesis of this kind of cobalt-imbedded zeolite catalyst. In short, the use of TPAOH and $NH_3 \cdot H_2O$ without involving any alkali metal cations can be significantly advantageous in the direct preparation of the cobalt-imbedded zeolite catalysts. Both $NH_4^+$ and $TPA^+$ cations can be occluded into the as-prepared catalysts to compensate the negative charge in the zeolite framework. When the as-synthesized catalysts were heated to remove the occluded organic complex of the template, the $NH_4^+$ decomposed as well, thus the protonic-form of the zeolite could be directly obtained upon calcinations. We also attempted to synthesize the catalysts with no template addition of the hydrothermal preparation, but no zeolite could be obtained.

During the hydrothermal process, the silica from the Co/$SiO_2$ precursor served as the only silica "nutrition", dissolving gradually and further in quantity up to a point where almost all Si was consumed in the procedure of the zeolite crystallization, meanwhile the added Al species were incorporated into the zeolite framework with the template action of the structure-directing reagent tetrapropylammonium hydroxide (TPAOH). In this case, the optimum basicity of the reaction system could be sufficiently regulated to dissolve Co/$SiO_2$ in a proper rate, and the remaining $Co_3O_4$ clusters served as substrates for the nucleation and growth of the zeolite crystals. In addition, the silica dissolving process should coincide with the zeolite crystallization process, so that the hydrogels containing silicon and aluminum groups could react properly to construct the zeolite framework. In a word, a "balance" or "synchronization" between the silica dissolving and the zeolite crystallization processes is the key to obtain this new-type cobalt-imbedded zeolite catalyst with high degree of crystallinity, in which cobalt oxide particles could be appropriately imbedded into the zeolite crystals. Therefore, the CoZ-xN catalysts with different ammonia addition in the synthetic solution are thoroughly investigated in this work since basicity is reasonably considered to play an extremely important role in the catalyst preparation process, as discussed above. With these findings, we can come to the following interpretations. If the addition of ammonia were not enough, the basicity of the synthesis system would be insufficient to dissolve the silica species from the Co/$SiO_2$ precursor. With increasing of the ammonia dosage, the basicity is increased and the kinetics of silica dissolution is accelerated, which is more and more inclined to coordinate the silica

dissolution and zeolite crystallization processes, and finally highly crystallized cobalt-imbedded zeolite catalyst can be prepared. However, some other deteriorative effects on the catalyst structure and zeolite acidity could arise if excessive ammonia were added, which will be further discussed later. In a word, with the preparation condition carefully regulated, the optimal catalyst with delicate cobalt-imbedded structure can be obtained as designed.

Based on these understandings and above discussions, we proposed the formation mechanism for the synthesis of the cobalt-imbedded zeolite catalyst. In the first stage, with proper and sufficient basicity, the $Co/SiO_2$ precursor is decomposed into small parts, as exhibited in the typical TEM image of the CoZ-300N sample treated at 453 K for the hydrothermal duration of 18 h (Fig. 6a). In the second stage, these dissolving silica species reacted with the added aluminum species to form the aluminosilicate framework with the help of the template TPAOH, thus the "intermediate" is generated (Fig. 6b). Finally, in the process of the remaining hydrothermal duration, the "intermediate" continues to interact with each other to form highly crystallized cobalt-imbedded zeolite catalyst as designed.

### *Reduction behavior of the catalysts*

The reduction performance of various catalysts was investigated by the hydrogen temperature-programmed reduction ($H_2$-TPR), with the profiles presented in Fig. 7. To better elucidate the reduction behavior of the samples, we divided the spectra into three regions. As shown in region I, two peaks are clearly distinguished, indicating that the reduction of $Co_3O_4$ to metallic Co can be identified as two consecutive stages with CoO as an intermediate [30]. Compared with all the zeolite-containing samples, the initiating and peak-maximum temperatures are the lowest for the $Co/SiO_2$

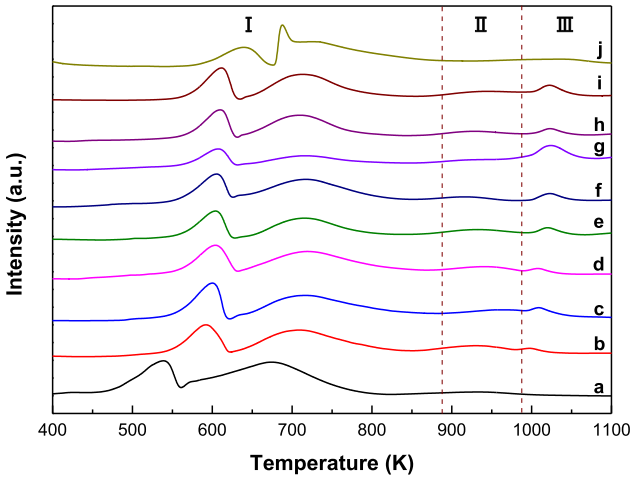


**Fig. 7 – $H_2$-TPR profiles of the catalysts: (a) $Co/SiO_2$, (b) CoZ-0N, (c) CoZ-15N, (d) CoZ-50N, (e) CoZ-100N, (f) CoZ-200N, (g) CoZ-300N, (h) CoZ-400N, (i) CoZ-500N and (j) Co/Z.**

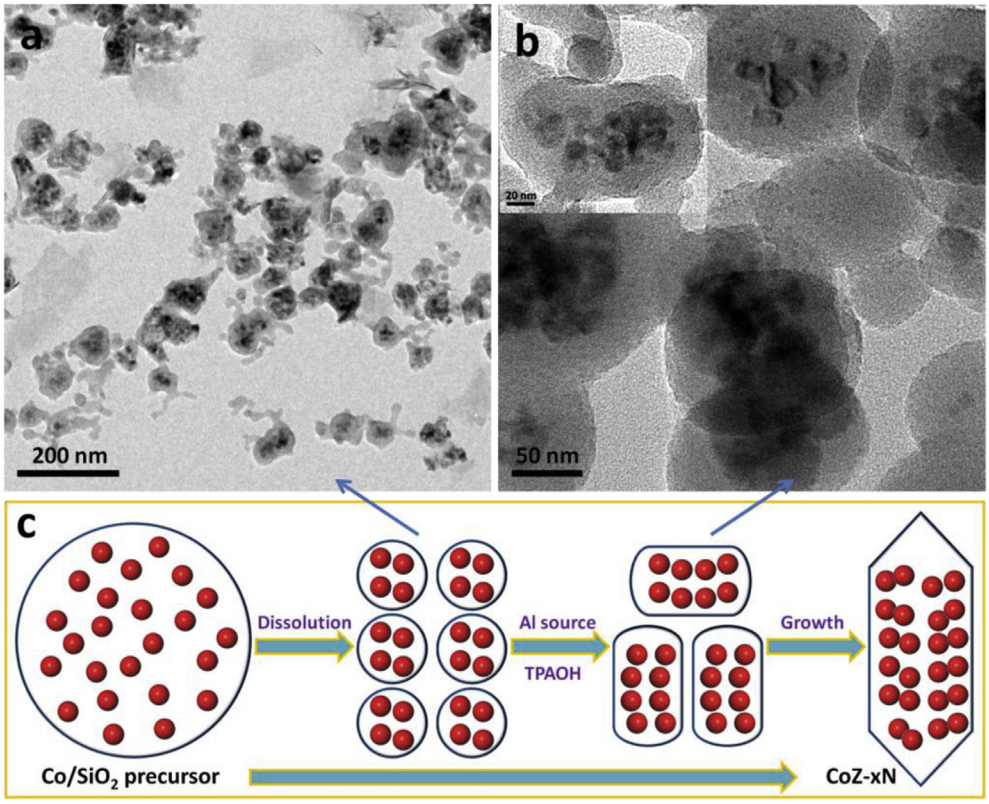


**Fig. 6 – TEM images of the samples treated at 453 K for different hydrothermal durations: (a) 18 h and (b) 50 h. The inset in (b) is a magnified image. (c) Schematic illustration of the proposed formation mechanism for the synthesis of the cobalt-imbedded zeolite catalyst.**

catalyst, revealing its outstanding reducibility, as expected from the relatively high cobalt content of 20 wt% and the weak interaction of cobalt nitrate with the silica support. For the CoZ-xN catalysts, the shape of the reduction profiles in this region resembled with that of the $Co/SiO_2$ catalyst, which can be reflected from the similar $Co_3O_4$ size (Table 1). Furthermore, in comparison with the $Co/SiO_2$ catalyst, the increase of the initiating temperatures of the CoZ-xN catalysts can be rationally explained when the cobalt-imbedded structure and the diffusion restraint of hydrogen among the microporous zeolite channels are considered. For the Co/Z catalyst, the reduction of $Co_3O_4$ to CoO is significantly retarded. Moreover, the second reduction peak with regard to the reduction of CoO to Co is quite broad, spanning from 660 K to 900 K, indicating its lowest reducibility. These observations from the Co/Z catalyst can be ascribed to the extremely strong interaction of metal oxides with the HZSM-5 support, considering its smallest cobalt particle size. Khodakov et al. [31] demonstrated that smaller cobalt particles have more intensive interaction with the catalyst support. This strong mutual interaction and consequent large resistance for reduction, was also found in the report of Kang et al., with the same cobalt loading and zeolite [7]. In region II, all the samples showed a rather weak and broad peak, implying the existence of hardly reducible components, such as cobalt aluminates or silicates [32]. Nevertheless, no assignment for these species could be readily ascertained by the XRD analysis due to their trace content in the catalyst.

The initiating temperatures of the CoZ-xN catalysts are not in evident difference or good regularity. However, in region III, it is interesting to find that another distinguishable peaks with markedly different intensity centered at about 1050 K appear for all the CoZ-xN catalysts. It is believed that the appearance of this additional peak characterizes the imbedment-structured catalyst, and can be attributed to the complex irreducible compounds derived from the strong mutual interaction of cobalt with HZSM-5 since the cobalt particles are imbedded into the zeolite crystals. The differences originate from the $H_2$-TPR results further confirm that the novel cobalt-imbedded catalyst consisting of cobalt component and zeolite material was successfully developed in our study, in accordance with the results of other characterization tools. Furthermore, as shown in region III, the intensity or area of the reduction peak increases gradually from CoZ-0N to CoZ-300N and then decreases, with CoZ-300N catalyst displaying the highest one, which exhibits the same trend with the variation of crystallinity. For CoZ-400N and CoZ-500N catalysts, the structure destruction due to the excess ammonia of the hydrothermal system, as stated above, should make the hydrogen reduction process easier to proceed than that of the CoZ-300N catalyst. These observations will be further discussed later, combined with the various Fischer–Tropsch reaction results.

### *Catalytic performances of the Fischer–Tropsch Synthesis*

#### *Catalytic activity*

The catalytic features of the series CoZ-xN catalysts were summarized in Table 2. To better elucidate the unique imbedment structure for the direct synthesis of gasoline-range hydrocarbons, the precursor $Co/SiO_2$ catalyst and the supported Co/Z catalyst were tested as well for a comparison purpose under the same FTS reaction conditions. As shown in Table 2, the conventional $Co/SiO_2$ catalyst shows a very high CO conversion of 95.7% as expected, which is very common under the reaction condition applied in this study. In the case of the Co/Z catalyst, however, extremely poor catalytic activity (CO conversion of only 18.1%) was obtained and can be ascribed to its poor reducibility, which means fewer $Co^0$ active sites were available during the Fischer–Tropsch process.

What's more, the diffusion barrier or limitation [33], which is strongly dependent on the structure feature of the catalyst, can seriously affect the diffusional access of CO and $H_2$ to the active sites. This means the syngas diffusion process also plays an important role in determining the FTS activity, similar to the hydrogen diffusion restriction in the $H_2$-TPR process as illustrated previously. Indeed, the diffusion effect can be of paramount significance in the catalytic process. Example of a quantitative calculation was given that a 1-fold increase in the diffusion length would lead to about 20-fold

**Table 2 – Comparison of the catalytic performance of different catalysts.[a]**

| Catalyst | Conv./% | Sel./%[b] | Sel./% | | | | | $\alpha$[c] | $C_{iso}/C_n$[d] | $C^=/C_n$[e] |
|---|---|---|---|---|---|---|---|---|---|---|
| | CO | $CO_2$ | $C_1$ | $C_2$–$C_4$ | $C_5$–$C_{12}$ | $C_{13}$–$C_{20}$ | $C_{20+}$ | | | |
| $Co/SiO_2$ | 95.7 | 14.3 | 22.5 | 19.6 | 44.8 | 12.4 | 0.72 | 0.82 | 0.12 | 0.10 |
| CoZ-0N | 84.2 | 8.34 | 29.6 | 21.8 | 45.4 | 2.95 | 0.25 | 0.78 | 0.31 | 0.14 |
| CoZ-15N | 80.5 | 6.79 | 28.1 | 20.8 | 49.0 | 2.02 | 0.07 | 0.75 | 0.42 | 0.23 |
| CoZ-50N | 78.6 | 6.48 | 26.6 | 20.0 | 51.5 | 1.86 | 0.02 | 0.74 | 0.81 | 0.28 |
| CoZ-100N | 76.9 | 6.02 | 22.5 | 15.7 | 61.0 | 0.77 | 0 | 0.73 | 1.71 | 0.30 |
| CoZ-200N | 74.7 | 3.39 | 19.0 | 10.6 | 69.7 | 0.66 | 0 | 0.79 | 3.17 | 0.30 |
| CoZ-300N | 65.4 | 2.41 | 22.3 | 15.2 | 62.3 | 0.25 | 0 | 0.78 | 4.55 | 0.36 |
| CoZ-400N | 72.4 | 4.30 | 26.6 | 19.0 | 53.8 | 0.56 | 0 | 0.75 | 2.03 | 0.25 |
| CoZ-500N | 76.3 | 5.05 | 29.3 | 21.4 | 48.3 | 1.05 | 0 | 0.73 | 1.32 | 0.22 |
| Co/Z | 18.1 | 9.07 | 37.0 | 37.1 | 25.9 | 0 | 0 | 0.70 | 1.83 | 0.23 |

[a] Reaction conditions: 1.0 MPa, 533 K, molar ratio of $H_2/CO = 2.0$, $W/F = 5$ gcat h $mol^{-1}$ time on stream 30 h.
[b] Analyzed by TCD.
[c] Chain growth probability.
[d] The molar ratio of *iso*-paraffins to *n*-paraffins in the range of $C_5$–$C_{12}$.
[e] The molar ratio of olefins to *n*-paraffins with $C_{2+}$ hydrocarbons.

increase in the gas diffusion time in the mesopores of the SBA-15 materials [34]. In spite of the different zeolite type and reaction details, similar mechanism seems to be valid in this study. During the FTS reaction process, for the impregnated Co/Z catalyst, the external CO and $H_2$ molecules must diffuse along the narrow and long zeolite channels to contact the rather dispersed small cobalt particles in the zeolite crystals. Moreover, pore blocking induced by the tiny cobalt particles in the Co/Z catalyst can further aggravate the diffusion difficulty of syngas [35]. This diffusion behavior is significantly different from the all-around diffusion paths of the CoZ-300N catalyst with concentrated large $Co_3O_4$ clusters (Fig. 3c). Hence, the apparently large diffusion barrier as stated above serves to explain the low catalytic activity of the Co/Z catalyst activity from another aspect.

The catalytic activity of the series CoZ-xN catalysts ranges from 65.4% to 84.2%, indicating the significant effect of hydrothermal basicity on the catalyst properties. This effect is more strongly presented from CoZ-100N to CoZ-400N, with CO conversion dropping sharply from 74.7% for CoZ-200N catalyst to 65.4% for CoZ-300N as an example. Also, as shown in Fig. S3, it is interesting to find that the activity of the CoZ-xN catalysts presents a concave curve. That is, the CO conversion undergoes a first decrease from CoZ-0N to CoZ-300N and then an increase from CoZ-300N to CoZ-500N, which is in fairly agreement with the reduction capability of the catalysts as verified by TPR measurement. In addition, the cobalt particle size generally considered to have influences on the catalytic activity [36] should not be involved in the explanation of the different catalytic activities of CoZ-xN catalysts due to the slight variation of the cobalt sizes in the range of 9.8–10.4 nm.

Fig. 8 presents the variation of CO conversion with time-on-stream (TOS) of the catalysts. As for the cobalt-based FTS catalysts, the main deactivation reasons have been summarized as the follows: water-induced oxidation of cobalt, formation of compounds between cobalt and supports, sintering or cluster growth and finally refractory coke formation [37]. As expected, the $Co/SiO_2$ catalyst exhibits excellent stability

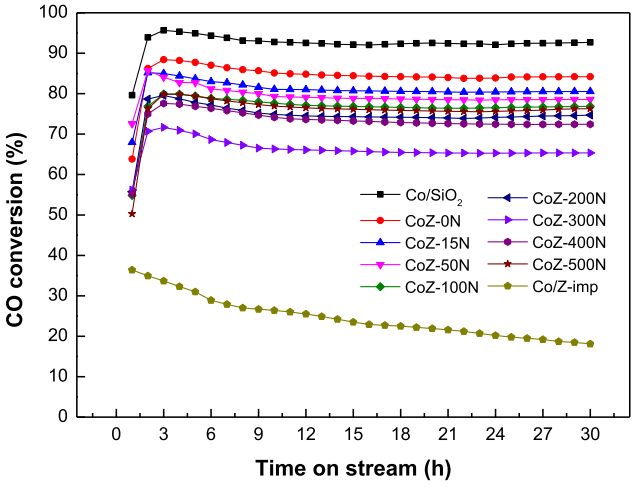


**Fig. 8 – CO conversion with time on stream over the various catalysts. Reaction conditions: 1.0 MPa, 533 K, molar ratio of $H_2/CO = 2.0$, $W/F = 5$ gcat h $mol^{-1}$, time on stream 30 h.**

during the reaction period, which can be explained by its high reducibility and large cobalt particles. It has been reported that cobalt particles with smaller sizes can be more inclined to be reoxidized and sintered by the water byproduct [38], and thus facilitate the generation of irreducible species, which are unstable and inactive during the reaction process. The gradual rate loss of catalytic activity during the first hours can be rationally ascribed to the accumulation of heavy hydrocarbons (waxes) and the progressive filling of liquid waxes in the pores, resulting in a weakened diffusion rate of syngas to react with the cobalt active sites located inside the pores [39]. The cracking of part of the long-chain hydrocarbons with an acidic co-catalyst in the hybrid system has been verified to slow down the deactivation rate and thus can improve the catalyst life time in the FTS process [11]. However, for the Co/Z catalyst with the acidic HZSM-5 as support, such a beneficial effect of the usage of zeolite on the catalytic stability was not observed. Instead, a fast deactivation behavior took place, which can be attributed to the easily reoxidized and sintered small cobalt particles initiated from the seriously retarded water removal process due to the mass transfer restrictions as mentioned above.

For the CoZ-xN catalysts, very different deactivation behaviors were observed. All the CoZ-xN catalysts display relatively stable CO conversion during the reaction period, which yet should originate from diverse reasons. For the CoZ-200N and 300N catalysts, the ideal cobalt-imbedded structure can bring a lot of advantages. On one hand, the larger cobalt particle size and the faster water removal rate derived from the low diffusion barrier as discussed previously can effectively suppress the reoxidizing and aggregating of cobalt particles, with more fine $Co^0$ active sites accessible for the CO and $H_2$ molecules. On the other hand, the long-chain hydrocarbons with low volatility, reported to dominate in the coke formation of HZSM-5 zeolite [10], can be sufficiently cracked and taken away to hinder the possible coke accumulation. With respect to the CoZ-0N to 100N catalysts, they seem to possess the mixture properties of the undissolved $Co/SiO_2$ catalyst and the cobalt-imbedded zeolite catalyst due to their low zeolite crystallinity, which can be reasonably applied to explain their stable catalytic activity. For the CoZ-400N and -500N catalysts, the FTS catalytic activity can be maintained to a large extent owing to the firm cobalt-imbedded structure in spite of the negative effects of excess ammonia addition, as indicated before.

*Product distribution*

The selectivity data of the catalysts were listed in Table 2 and presented in Fig. 9. The carbon number distribution of the $Co/SiO_2$ catalyst is very broad, with $C_{20+}$ produced, and only very small amounts of branched hydrocarbons are formed as indicated from the very low $C_{iso}/C_n$ molar ratio of 0.10 for the gasoline-range hydrocarbons. The relatively higher methane selectivity observed for the $Co/SiO_2$ catalyst can be attributed to the high reaction temperature employed in this study.

Compared with the $Co/SiO_2$ catalyst, all the zeolite-involved catalysts show a narrower product distribution. Such a positive effect originates from the hydrocracking and isomerization reactions of the long-chain hydrocarbons desorbing from the FTS active sites, with the help of the acidic

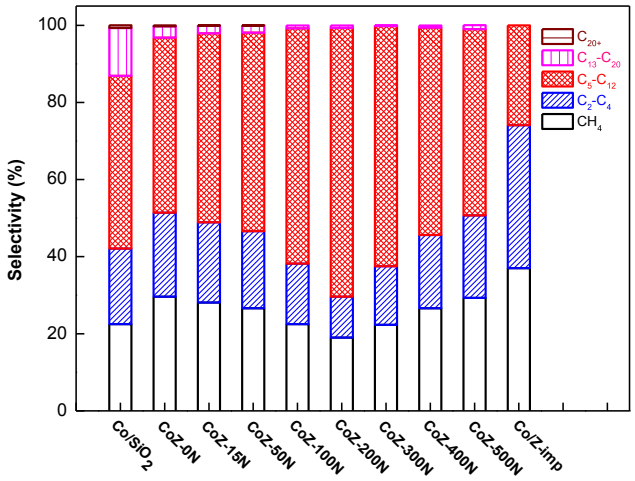


**Fig. 9 – Product distribution of the FTS reaction on the various catalysts. Reaction conditions: 1.0 MPa, 533 K, molar ratio of $H_2/CO = 2.0$, W/F = 5 gcat h $mol^{-1}$, time on stream 30 h.**

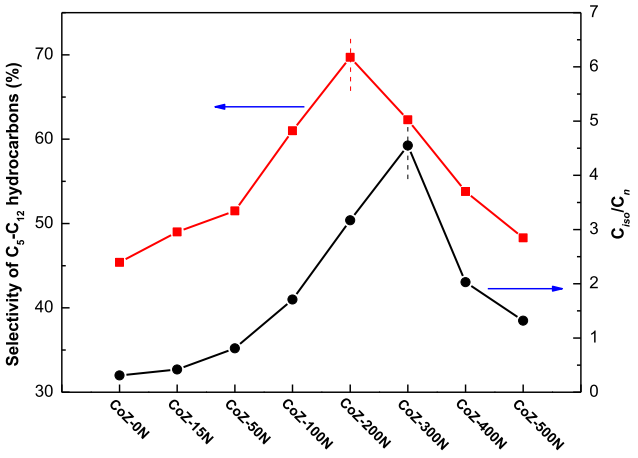


**Fig. 10 – Selectivity of $C_5$–$C_{12}$ hydrocarbons and $C_{iso}/C_n$ of the CoZ-xN catalysts. Reaction conditions: 1.0 MPa, 533 K, molar ratio of $H_2/CO = 2.0$, W/F = 5 gcat h $mol^{-1}$, time on stream 30 h.**

sites of the zeolite component. However, the highest $C_{iso}/C_n$ ratio was not achieved on the Co/Z catalyst, in spite of its most Brönsted acidic sites. This can be rationalized by the occurring of over-cracking [40], verified by the product distribution with completely avoided $C_{11+}$ hydrocarbons, which should be ascribed to the most acid sites of the zeolite and the prolonged residence time of the formed hydrocarbons diffusing along the zeolite channels derived from the mass transfer limitations. This is strongly supported by the high selectivity of $C_1$–$C_4$ light hydrocarbons for the Co/Z catalyst, with $CH_4$ of 37.0% and $C_2$–$C_4$ of 37.1%, respectively. Especially, methane is the least desired product for FTS, with numerous efforts devoted to reduce its selectivity [37]. The selectivity of methane (Fig. S3) can be affected by many factors, thus other reasons should also contribute to the extremely high $CH_4$ yield in the Co/Z catalyst. One is that the $H_2/CO$ ratio near the cobalt metal sites can be significantly higher than the original ratio from the external gas phase due to the severe diffusion barrier, as CO molecules diffusing much more slowly than $H_2$ [33]. Moreover, the unreduced cobalt oxide phase in the Co/Z catalyst as confirmed by the TPR experiment was reported to be able to catalyze the water-gas-shift (WGS) reaction ($CO + H_2O = CO_2 + H_2$), thus further increasing the effective $H_2/CO$ ratio [41]. This could be supported by the low $C^{=}/C_n$ value of the Co/Z catalyst in spite of the intensive cracking process. It should be noted that high $H_2/CO$ ratio is advantageous to the generation of $CH_4$ [41]. Moreover, smaller cobalt particles have the tendency to obtain higher selectivity of short-chain hydrocarbons, thus further promoting the $CH_4$ formation [42].

For the selectivity of gasoline-range ($C_5$–$C_{12}$) hydrocarbons, the lowest value is observed over the Co/Z catalyst due to its small cobalt size and the presence of over-cracking. Contrary to the contradiction in the Co/Z catalyst, it is interesting to find that the $C_5$–$C_{12}$ selectivity of the series CoZ-xN catalysts (Table 2 and Fig. 10) follows the expected trend of acidity tested by the $NH_3$-TPD experiments (Fig. 5), indicating that the secondary hydrocracking/isomerization reactions of the long-chain hydrocarbons were processed in different extents. Consequently, the highest gasoline selectivity of 69.7% and a $C_{iso}/C_n$ molar ratio of 3.17 were successfully obtained on the CoZ-200N catalyst. Compared with the Co/Z catalyst, the primary long-chain hydrocarbons of the CoZ-200N catalyst were firstly formed in abundance on the relatively large cobalt particles and then were effectively converted to the light and branched hydrocarbons via the secondary reactions along the zeolite channels with proper acidic sites. The confined reaction environment originated from the cobalt-imbedded structure and the high diffusion efficiency of the feed gas and the formed *iso*-paraffins significantly facilitated the selectivity of $C_5$–$C_{12}$ hydrocarbons for the CoZ-200N catalyst. However, the maximum $C_{iso}/C_n$ ratio was not found on the CoZ-200N catalyst. As observed in Fig. 10, the highest $C_{iso}/C_n$ ratio was obtained on the CoZ-300N catalyst, suggesting that the secondary reactions were conducted to a greater degree and therefore more *iso*-paraffins were produced. This can be reasonably ascribed to the present of more Brönsted acidic sites in the CoZ-300N catalyst than in the CoZ-200N catalyst.

As for the $CO_2$ selectivity, cobalt-based catalysts have been proved to show a low activity for the WGS reaction [2]. With the increase of the CO Conversion, the WGS reaction can be enhanced due to the more produced water, thus the selectivity of $CO_2$ will increase accordingly [37]. The $CO_2$ selectivity of 14.3% of the base $Co/SiO_2$ catalyst is understandable and common due to the high reaction temperature employed in this study. Nevertheless, the impregnated Co/Z catalyst presents a high $CO_2$ selectivity, despite its low catalytic reactivity. Such finding is not surprising when the catalyst structure and the reducibility are taken into consideration, based on the above results and discussion. As mentioned above, the WGS reaction can be remarkably enhanced due to the retarded evacuation of the generated water. Additionally, the unreduced cobalt oxides can catalyze the WGS reaction as mentioned above for the Co/Z catalyst, thus further promoting the $CO_2$ formation. What's worse, as previously discussed, the

slow water removal process tends to reoxidize the small cobalt particles, and then the WGS reaction will be further accelerated, which can be corroborated by the fast deactivation of the Co/Z catalyst. For the CoZ-xN catalyst, the $CO_2$ selectivity appears to be less than 8.34%, indicating the high utilization efficiency of CO, which can be regarded as an advantage considering the harmful impact of $CO_2$ on the global climate as a kind of greenhouse gas. It's also interesting to find that the variation trend of $CO_2$ selectivity corresponds with that of the CO conversion of the CoZ-xN catalysts. Owing to the fast evacuation of the formed water and large cobalt size, the detrimental effect of water on the CoZ-xN catalysts is significantly alleviated.

## Conclusions

By systematically regulating the hydrothermal condition, we have successfully prepared the cobalt-imbedded zeolite catalyst in which the $Co_3O_4$ particles are compatibly imbedded or confined into the HZSM-5 crystals. A series of catalysts with significantly different structure features, acidic properties and reduction behaviors were synthesized and tested with various characterizations. Ammonium hydroxide was reasonably selected and proved to be the proper alkali source for the hydrothermal preparation. The proton-type zeolite of the cobalt-imbedded zeolite catalyst can be directly obtained upon calcination without needing the conventional tedious ion-exchange process. In addition, the formation mechanism of the synthesis of the cobalt-imbedded catalyst was proposed. The coincidence of the rate of the silica dissolving process of the precursor Co/$SiO_2$ and the zeolite crystallization process is the crucial factor to the rational design of this imbedment-structured catalyst. The CoZ-xN catalysts were employed for the direct synthesis of gasoline-range hydrocarbons. It was observed that the optimal CoZ-xN catalysts remarkably promoted the gasoline selectivity and exhibited high catalytic activity and good stability. The highest gasoline selectivity was obtained on the CoZ-200N catalyst and the maximum $C_{iso}/C_n$ molar ratio was achieved on the CoZ-300N catalyst. These excellent catalytic performances were rationally attributed to the confined reaction environment derived from the cobalt-imbedded structure, the high diffusion efficiency, the proper reduction behavior, and the secondary reactions (hydrocracking, isomerization, etc) performed on the acidic sites of the H-type ZSM-5 zeolite. This tailor-made cobalt-imbedded zeolite catalyst provides a new route to the rational design of FTS catalyst with good catalytic activity, excellent reaction stability and high gasoline selectivity, and also has a great potential to be extended to other catalytic processes.

## Acknowledgements

This work was financially supported by the National Natural Science Foundation of China (91334206 and 21436001), the National "863" Program of China (No. 2012AA051001 and 2013AA031702), the Fundamental Research Funds for the Central Universities (BUCTRC201601 and JD1606), and the High-level Talents Research Fund of Yangzhou University.

## Appendix A. Supplementary data

Supplementary data related to this article can be found at http://dx.doi.org/10.1016/j.ijhydene.2016.10.004.

## REFERENCES

[1] Khodakov AY, Chu W, Fongarland P. Advances in the development of novel cobalt Fischer–Tropsch catalysts for synthesis of long–chain hydrocarbons and clean fuels. Chem Rev 2007;107:1692–744.
[2] Zhang Q, Kang J, Wang Y. Development of novel catalysts for Fischer–Tropsch synthesis: tuning the product selectivity. ChemCatChem 2010;2:1030–58.
[3] Yu S, Zhang T, Xie Y, Wang Q, Gao X, Zhang R, et al. Synthesis and characterization of iron-based catalyst on mesoporous titania for photo-thermal F-T synthesis. Int J Hydrogen Energy 2015;40:870–7.
[4] Forghani AA, Elekaei H, Rahimpour MR. Enhancement of gasoline production in a novel hydrogen-permselective membrane reactor in Fischer–Tropsch synthesis of GTL technology. Int J Hydrogen Energy 2009;34:3965–76.
[5] Haghtalab A, Mosayebi A. Co@Ru nanoparticle with core–shell structure supported over γ-Al2O3 for Fischer–Tropsch synthesis. Int J Hydrogen Energy 2014;39:18882–93.
[6] Stencel JM, Rao VUS, Diehl JR, Rhee KH, Dhere AG, DeAngelis RJ. Dual cobalt speciation in Co/ZSM–5 catalysts. J Catal 1983;84:109–18.
[7] Kang SH, Ryu JH, Kim JH, Sai Prasad PS, Bae JW, Cheon JY, et al. ZSM–5 supported cobalt catalyst for the direct production of gasoline range hydrocarbons by Fischer–Tropsch synthesis. Catal Lett 2011;141:1464–71.
[8] Li X, Luo M, Asami K. Direct synthesis of middle iso–paraffins from synthesis gas on hybrid catalysts. Catal Today 2004;89:439–46.
[9] Martínez A, López C. The influence of ZSM–5 zeolite composition and crystal size on the in situ conversion of Fischer–Tropsch products over hybrid catalysts. Appl Catal A 2005;294:251–9.
[10] Martínez A, Rollán J, Arribas MA, Cerqueira HS, Costa AF, S–Aguiar EF. A detailed study of the activity and deactivation of zeolites in hybrid Co/$SiO_2$–Zeolite Fischer–Tropsch catalysts. J Catal 2007;249:162–73.
[11] He J, Liu Z, Yoneyama Y, Nishiyama N, Tsubaki N. Multiple–functional capsule catalysts: a tailor-made confined reaction environment for the direct synthesis of middle isoparaffins from syngas. Chem Eur J 2006;12:8296–304.
[12] Bao J, He J, Zhang Y, Yoneyama Y, Tsubaki N. A core/shell catalyst produces a spatially confined effect and shape selectivity in a consecutive reaction. Angew Chem Int Ed 2008;47:353–6.
[13] Yang G, He J, Zhang Y, Yoneyama Y, Tan Y, Han Y, et al. Design and modification of zeolite capsule catalyst, a confined reaction field, and its application in one–step isoparaffin synthesis from syngas. Energy Fuels 2008;22:1463–8.
[14] Liu JY, Chen JF, Zhang Y. Cobalt–imbedded zeolite catalyst for direct syntheses of gasoline via Fischer–Tropsch synthesis. Catal Sci Technol 2013;3:2559–64.

[15] Liu JY, Chen JF, Zhang Y. Direct synthesis of Co@Al–MCM–41 catalyst from conventional Co/$SiO_2$ catalyst. RSC Adv 2015;5:62931–5.
[16] Ren N, Bronić J, Subotić B, Lv XC, Yang ZJ, Tang Y. Controllable and SDA–free synthesis of sub–micrometer sized zeolite ZSM–5. Part 1: influence of alkalinity on the structural, particulate and chemical properties of the products. Microporous Mesoporous Mater 2011;139:197–206.
[17] Fang Y, Hu H. Mesoporous TS–1: nanocasting synthesis with CMK–3 as template and its performance in catalytic oxidation of aromatic thiophene. Catal Commun 2007;8:817–20.
[18] Xue T, Wang YM, He MY. Facile synthesis of nano–sized $NH_4$–ZSM–5 zeolites. Microporous Mesoporous Mater 2012;156:29–35.
[19] Sazama P, Wichterlova B, Dedecek J, Tvaruzkova Z, Musilova Z, Palumbo L, et al. FTIR and $^{27}$Al MAS NMR analysis of the effect of framework Al–and Si–defects in micro–and micro–mesoporous H–ZSM–5 on conversion of methanol to hydrocarbons. Microporous Mesoporous Mater 2011;143:87–96.
[20] Klinowski J, Thomas JM, Fyfe CA, Gobbi GC. Monitoring of structural changes accompanying ultrastabilization of faujasitic zeolite catalysts. Nature 1982;296:533–6.
[21] Luan Z, Cheng CF, Zhou W, Klinowski J. Mesopore molecular sieve MCM–41 containing framework aluminum. J Phys Chem 1995;99:1018–24.
[22] Tago T, Konno H, Sakamoto M, Nakasaka Y, Masuda T. Selective synthesis for light olefins from acetone over ZSM–5 zeolites with nano–and macro–crystal sizes. Appl Catal A 2011;403:183–91.
[23] Wang Z, Wang L, Jiang Y, Hunger M, Huang J. Cooperativity of Brønsted and Lewis acid sites on zeolite for glycerol dehydration. ACS Catal 2014;4:1144–7.
[24] Corma A, Garcia H. Lewis acids: from conventional homogeneous to green homogeneous and heterogeneous catalysis. Chem Rev 2003;103:4307–66.
[25] Barrer RM. Hydrothermal chemistry of zeolites. London: Academic Press; 1982.
[26] Verhoef MJ, Kooyman PJ, van der Waal JC, Rigutto MS, Peters JA, van Bekkum H. Partial transformation of MCM–41 material into zeolites: formation of nanosized MFI type crystallites. Chem Mater 2001;13:683–7.
[27] An X, Wu B, Hou W, Wan H, Tao Z, Li T, et al. The negative effect of residual sodium on iron–based catalyst for Fischer–Tropsch synthesis. J Mol Catal A Chem 2007;263:266–72.
[28] Kim SD, Noh SH, Park JW, Kim WJ. Organic–free synthesis of ZSM–5 with narrow crystal size distribution using two–step temperature process. Microporous Mesoporous Mater 2006;92:181–8.
[29] Abelló S, Bonilla A, Pérez–Ramírez J. Mesoporous ZSM–5 zeolite catalysts prepared by desilication with organic hydroxides and comparison with NaOH leaching. Appl Catal A 2009;364:191–8.
[30] Lv J, Ma X, Bai S, Huang C, Li Z, Gong J. Hydrogenation of carbon monoxide over cobalt nanoparticles supported on carbon nanotubes. Int J Hydrogen Energy 2011;36:8365–72.
[31] Khodakov AY, Griboval–Constant A, Bechara R, Zholobenko VL. Pore size effects in Fischer Tropsch synthesis over cobalt–supported mesoporous silicas. J Catal 2002;206:230–41.
[32] Sexton BA, Hughes AE, Turney TW. An XPS and TPR study of the reduction of promoted cobalt–Kieselguhr Fischer–Tropsch catalysts. J Catal 1986;97:390–406.
[33] Vervloet D, Kapteijn F, Nijenhuis J, van Ommen JR. Fischer–Tropsch reaction–diffusion in a cobalt catalyst particle: aspects of activity and selectivity for a variable chain growth probability. Catal Sci Technol 2012;2:1221–33.
[34] Prieto G, Martínez A, Murciano R, Arribas MA. Cobalt supported on morphologically tailored SBA–15 mesostructures: the impact of pore length on metal dispersion and catalytic activity in the Fischer–Tropsch synthesis. Appl Catal A 2009;367:146–56.
[35] Coronel-García MA, de la Torre AIR, Melo-Banda JA, Martínez-Salazar AL, Rodrigo RS, Zavala NPD, et al. Study of Co, Ru/SBA-15 type materials for Fischer–Tropsch synthesis in fixed bed tubular reactor: I. Effect of the high Ru content on the catalytic activity. Int J Hydrogen Energy 2015;40:17264–71.
[36] Den Breejen JP, Radstake PB, Bezemer GL, Bitter JH, Frøseth V, Holmen A, et al. On the origin of the cobalt particle size effects in Fischer–Tropsch catalysis. J Am Chem Soc 2009;131:7197–203.
[37] Tsakoumis NE, Rønning M, Borg Ø, Rytter E, Holmen A. Deactivation of cobalt based Fischer–Tropsch catalysts: a review. Catal Today 2010;154:162–82.
[38] Iglesia E. Design, synthesis, and use of cobalt–based Fischer–Tropsch synthesis catalysts. Appl Catal A 1997;161:59–78.
[39] Post MFM, Van't Hoog AC, Minderhoud JK, Sie ST. Diffusion limitations in Fischer–Tropsch catalysts. AlChE J 1989;35:1107–14.
[40] de Klerk A. Thermal cracking of Fischer–Tropsch waxes. Ind Eng Chem Res 2007;46:5516–21.
[41] Bao A, Liew K, Li J. Fischer–Tropsch synthesis on CaO–promoted Co/$Al_2O_3$ catalysts. J Mol Catal A Chem 2009;304:47–51.
[42] Bezemer GL, Bitter JH, Kuipers HPCE, Oosterbeek H, Holewijn JE, Xu X, et al. Cobalt particle size effects in the Fischer–Tropsch reaction studied with carbon nanofiber supported catalysts. J Am Chem Soc 2006;128:3956–64.